Title page

Brief excitotoxic insults cause a calpain-mediated increase in nuclear membrane permeability in neonatal neurons.

Authors and affiliations:

P. Suryavanshi[1,2], R. Langton[1,2], K. Fairhead[3] and J. Glykys[1,2,4,]

[1] Department of Pediatrics, University of Iowa, Iowa City, IA.

[2] Iowa Neuroscience Institute, University of Iowa, Iowa City, IA.

[3] Biomedical Sciences, College of Liberal Arts and Sciences, University of Iowa, Iowa City, IA.

[4] Department of Neurology, University of Iowa, Iowa City, IA.

Corresponding author:

Dr. Joseph Glykys

Address: 2324 PBDB, 169 Newton Road, Iowa city, Iowa 52242

Email: joseph-glykys@uiowa.edu

Conflict of interest statement

The authors declare no competing interests.

Abstract

Neuronal edema after excitotoxic brain insults results in neuronal injury and death. Osmotic and surgical interventions designed to mitigate edema yield poor clinical outcomes, highlighting the need to explore other mechanisms. Concurrent with neuronal swelling, excessive Ca^{2+} loading can be deleterious but remains poorly investigated, especially during the neonatal period. We used *in* and *ex vivo* multiphoton Ca^{2+} imaging to evaluate the relationship between cytotoxic edema and Ca^{2+} load in neonatal GCaMP6-expressing neurons after different and brief excitotoxic insults. We report acute translocation of cytosolic GCaMP6s into the nucleus of neonatal neurons after various short excitotoxic insults quantified as the ratio of nuclear: cytosolic intensity (N/C ratio). The increase in the N/C ratio occurred independently of neuronal swelling. Transmission electron microscopy revealed that elevated N/C ratios correlated with increased nuclear pore size in neurons. Inhibiting calpains *in* and *ex vivo* prevented increased N/C ratios and decreased neuronal swelling. Our results demonstrate that brief excitotoxic injury can enlarge nuclear pores and dysregulate nuclear transport in neurons through a calpain-mediated mechanism during early brain development. Additionally, N/C ratio measurements can be used to detect acute neuronal injury in real-time.

Graphical abstract

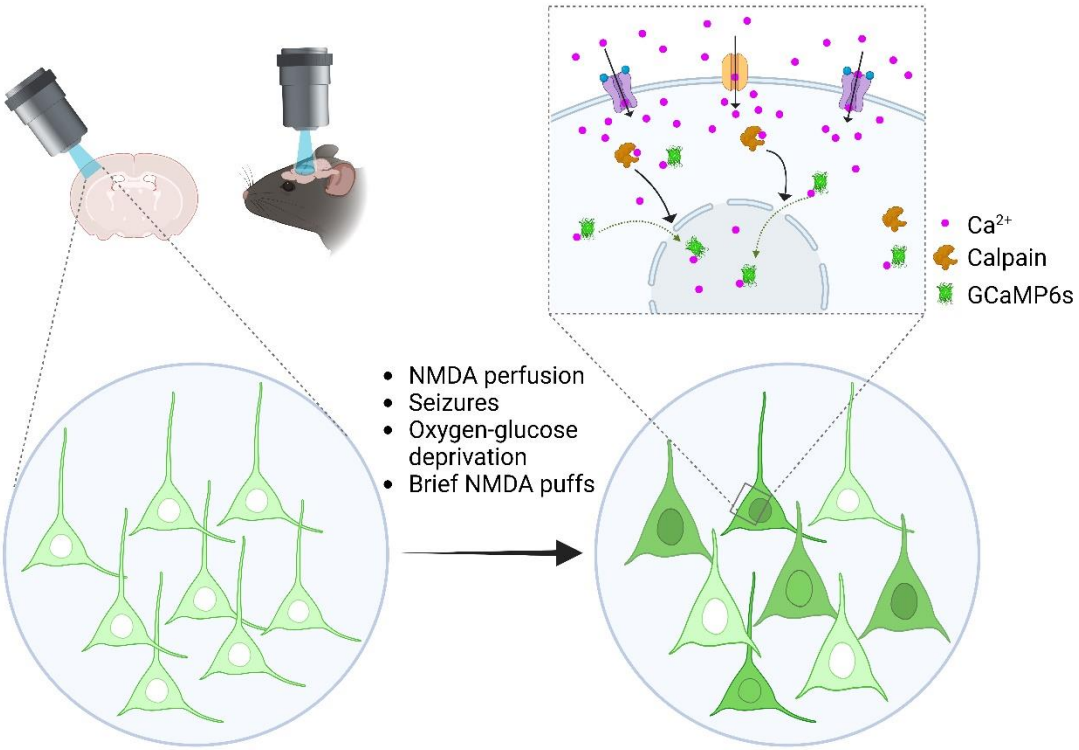

Main Text

Introduction

Multiple brain insults, including stroke, hypoxia, prolonged seizures, and traumatic brain injury, cause brain swelling, leading to severe morbidity or death(1–4). Osmotic and surgical interventions employed to mitigate cellular edema continue to yield poor outcomes(5, 6), suggesting that mechanisms independent of brain swelling may contribute to cell injury and death(4, 5, 7). Notably, there is a lack of therapeutic strategies targeting neonates and children, and current treatments have been extrapolated from adult studies. Thus, there is a critical need to understand the downstream consequences of excitotoxic injury leading to poor outcomes, especially in pediatric patients.

In addition to swelling, excitotoxic insults can induce intracellular Ca^{2+} elevation in neurons(8). Rapid neuronal Ca^{2+} influx following neuronal activity and excitotoxic Ca^{2+} overload can be visualized using genetically encoded, fluorescent Ca^{2+} indicators (GECIs) like GCaMPs, even in subcellular compartments of neural populations(9, 10). An unintended and less explored 'side-effect' of the expression of cytosolically restricted GCaMP is its abnormal nuclear accumulation during injury(11). Without nuclear localization signals, macromolecules like GCaMPs (~70 kD) are restricted to the cytosol, as only smaller proteins can permeate the nucleus through passive diffusion(12, 13). Therefore, nuclear accumulation of typically cytosolic GCaMPs implies altered nuclear membrane permeability, often associated with cytotoxic cell death(14–16). Moreover, neurons with GCaMP-filled nuclei show altered physiology(17, 18). However, previous reports indicate that nuclear membrane breakdown and consequent nuclear accumulation of macromolecules is a slow process that typically requires prolonged exposure to supraphysiological insults.

In this study, we demonstrate an acute, calpain-dependent nuclear translocation of GCaMP6s following brief, physiologically relevant excitotoxic insults (some associated with cytotoxic edema), both *in vitro*

and *in vivo*. Nuclear translocation of GCaMP6s was associated with enlarged nuclear pores in neonatal mouse (P8-12) neocortical neurons. Our results demonstrate that the abnormal translocation of GCaMP6s to the nucleus following excitotoxic insults is gradual, in the timeframe of minutes, and independent of neuronal swelling, pointing to dysregulation of protein localization in injured neurons. Our results shed light on some reasons for the lack of good clinical outcomes even after mitigating brain swelling. Additionally, since the expression of biomarkers associated with neuronal death and injury is typically delayed (hours to days), we also propose that this abnormal nuclear translocation can be a useful tool for the early detection of neuronal injury.

Results

Brief NMDA exposure induces long-term neuronal swelling and Ca^{2+} elevation in neonatal brain slices.

We first evaluated the consequences of brief excitotoxic injury induced by excessive NMDAR activation, commonly observed in multiple pathological insults, on neuronal swelling and Ca^{2+} dynamics in mouse neocortical neurons (layer IV/V) *in vitro* during the neonatal period (P8-12). A brief application of NMDA (30 µM for 10 min) induced hyperexcitability and prolonged neuronal Ca^{2+} elevation imaged by multiphoton microscopy (Thy1-GCaMP6s, **Supplemental Figure 1A, B**). This brief NMDA application also resulted in varicose swelling or beading of dendrites (Thy1-YFP, **Supplemental Figure 1C**).

To simultaneously image neuronal edema and Ca^{2+} activity, we expressed a neuron-specific stable fluorophore (mRuby2) and a Ca^{2+} sensor (GCaMP6s)(19), using intraventricular AAV injections(20) in newborn pups (P0-2; **Figure 1A**). Neuronal fluorophore expression was evident at 7 days post-injection. Neuronal areas were measured using an automated convolutional neuronal network algorithm (ANMAF; **Figure 1A**) which detects and measures neuronal size while avoiding human bias in the area determination(21). NMDA application triggered synchronized Ca^{2+} transients in neurons that transitioned to persistently high Ca^{2+} during 40 min of washout (**Figure 1B and C, Video 1**). NMDA perfusion

also caused a persistent increase in neuronal area (**Figure 1D, Supplemental Figure 2A-D**). Ca^{2+} elevation had a weak but significant correlation with swelling during but not after NMDA perfusion (**Supplemental Figure 2E**). Notably, there was no significant difference when either GCaMP6s or mRuby2 was used to measure changes in neuronal size (**Figure 1D**).

As neuronal swelling measurements were similar between mRuby2 and GCaMP6s, we turned to transgenic mice expressing GCaMP6s in a subset of neocortical neurons (Thy1-GCaMP6s) for the rest of our experiments (**Figure 1E**). We confirmed that brief NMDA application in neonatal acute brain slices from Thy1-GCaMP6s mice (P8-12) caused long-term neuronal swelling (**Figure 1F and G**) in a subset of neurons. In contrast, others showed either resistance to NMDA-induced excitotoxicity or a return to baseline (**Figure 1H-I, Supplemental Figure 3C**). NMDA-induced neuronal swelling and $[Ca^{2+}]_i$ elevation were blocked by the NMDA receptor antagonist, AP5. Swelling and elevated $[Ca^{2+}]_i$ were also absent during prolonged perfusion with artificial cerebrospinal fluid (aCSF, **Figure 1G-I, Supplemental Figure 3A-C**), suggesting that the persistent swelling and Ca^{2+} elevation are caused by transient NMDA receptor activation. With aCSF, but not AP5, there was a slight decrease in the neuronal area over time, possibly due to the osmolarity of aCSF (300 mOsm). In summary, these results show that excitotoxic neuronal swelling and Ca^{2+} elevation occur concurrently, and that neuronal area can be measured with GCaMP6s.

Excitotoxic injury causes GCaMP6s translocation into the nucleus of neonatal neurons.

Although GCaMPs are widely used GECIs due to their rapid response kinetics and good signal-to-noise ratio(9), multiple reports show an abnormal nuclear accumulation of GCaMP in unhealthy or injured neurons(11, 17). We only observed “injured” neurons with GCaMP-filled nuclei in the superficial tissue of our acute slices (~0 to 40 µm from the surface; **Supplemental Figure 1D**). Thus, we restricted our imaging to healthy neurons (cytosolic GCaMP6s expression) located at 80-200 µm below the slice surface. Interestingly, we observed gradual GCaMP6s translocation to the nucleus in a subgroup of

neurons following NMDA application, even at optimal imaging depths (**Figure 2A**). To quantify the changes in nuclear GCaMP6s intensity, we normalized the nuclear to the cytosolic GCaMP6s fluorescence (N/C ratio), using compartmentalized ROIs (**Figure 2B**). The N/C ratio was unchanged in neurons under prolonged aCSF perfusion yet was significantly increased after NMDA perfusion and prevented by AP5 (**Figure 2C-E**). The elevation in the N/C ratio began shortly after NMDA treatment and persisted for the duration of the experiment (~30 minutes, **Supplemental Figure 4A-D**). The N/C ratio did not correlate to changes in neuronal size (at 10 and 40 minutes, **Figure S2F**). However, the increased N/C ratio was significantly correlated to an increase in Ca^{2+} load at 40 minutes (ΔN/C ratio vs. ΔGreen/Red ratio, **Figure 2F**), suggesting a possible Ca^{2+}-mediated mechanism underlying the NMDA-induced increase in the N/C ratio. Interestingly, the N/C ratio increased in some neurons that shrank during aCSF perfusion alone (at 40 minutes, **Supplemental Figure 3D**), further negating a causal relationship between the degree of neuronal swelling and elevated N/C ratio.

Since neurons undergo trauma during brain slice preparation(22), we evaluated if N/C elevation following an excitotoxic insult also occurs *in vivo.* We performed multiphoton imaging in anesthetized neonatal Thy1-GCaMP6s mice (P11-17) during baseline, application of an NMDA-containing saline solution (500 µM, 10 min) over the craniotomy site, and after washout (**Figure 3A**). As seen in acute brain slices, NMDA caused significant and prolonged neuronal swelling and increased the N/C ratio *in vivo* (**Figure 3B-D, Supplemental Figure 4F; Video 2**). Hence, nuclear translocation of GCaMP6s occurs after cytotoxic edema induced by excessive NMDAR activation, both *in vivo* and *in vitro*.

Next, we performed control experiments to evaluate if the observed N/C elevation is an artifact caused by putative saturation of the GCaMP6s signal resulting from the intense neuronal stimulation and massive Ca^{2+} influx during NMDA application. First, we evaluated the N/C ratio change using the isosbestic point of GCaMP6s (810 nm, Ca^{2+}-independent two-photon excitation) *in vitro* (Akam and Walton, 2019). Electrical stimulus-evoked responses increased the GCaMP6s signal at 920nm excitation and

diminished fluorescence at isosbestic excitation (**Supplemental Figure 5A, B; Video 3**). NMDA resulted in neuronal swelling in the same slices using both excitation wavelengths (**Supplemental Figure 5C, D**). More importantly, the elevation of the N/C ratio was observed in the same slices after NMDA application using both excitation wavelengths (**Supplemental Figure 5E**). Thus, we conclude that the increase in N/C is not an artifact of signal saturation but a physiological anomaly.

Second, depending on the laser intensity and duration of exposure, multiphoton imaging can induce varying degrees of phototoxicity(24), which could contribute to elevated N/C ratios. To address this, we applied NMDA (30 µM, 10 min) to acute brain slices, and instead of undergoing multiphoton imaging, they were fixed ~2 hours after NMDA application, embedded for cryo-sectioning, and the neuronal GCaMP6s signal was imaged using epifluorescence microscopy (**Figure 3E**). We again observed a marked elevation in the number of neurons with GCaMP-filled nuclei in NMDA-treated sections compared to the aCSF control (**Figure 3F**). Together, these results indicate that the elevation in the N/C ratio is due to the entry of GCaMP6s into neuronal nuclei.

Different neocortical insults increase the N/C ratio in the neonatal brain.

Robust NMDA receptor activation occurs during prolonged refractory seizures or asphyxia/anoxic depolarizations(25–27), which can be cytotoxic(28, 29) or result in neuronal death(30). Thus, we evaluated if nuclear GCaMP6s translocation, observed during brief NMDA exposure, also occurs with other excitotoxic insults.

First, we used repeated short NMDA puffs (3x100 ms) to mimic synchronous network stimulation. The NMDA puffs evoked reproducible Ca^{2+} transients in Thy1-GCaMP6s acute brain slices (P8-12 neocortex, **Figure 4A, B; Video 4**). Neurons did not swell after multiple NMDA puffs, yet the N/C ratio increased with repeated stimulations, becoming significantly high after 8-10 stimuli (**Figure 4C**).

Second, we measured the neuronal N/C ratio during seizure-like activity in P8-12 neocortical slices perfused with a K^+ channel blocker 4-Aminopyridine (4-AP) for 70-80 minutes while performing multiphoton imaging (**Figure 4D**). We observed synchronous, prolonged Ca^{2+} spikes with 4-AP (**Figure 4E, Video 5**). Z-stack images acquired during inter-ictal periods demonstrated a significant increase in the N/C ratio in neurons starting 10 min after seizure-like activity lasting throughout the experiment (~70 minutes, **Figure 4F**). Early on, we did not observe neuronal swelling. However, it was apparent at 70 mins (**Figure 4F**).

Third, we evaluated if oxygen-glucose deprivation (OGD) leads to a high neuronal N/C ratio. OGD is a hallmark feature of neurological conditions like ischemic-hemorrhagic stroke, brain trauma, and asphyxiation-hypoxia(31, 32). We induced prolonged or brief OGD (reperfusion) in Thy1-GCaMP6s brain slices while performing multiphoton imaging (**Supplemental Figure 6A**). The effect of OGD was confirmed by the induction of anoxic depolarizations (AD) spreading across the neonatal neocortex (**Supplemental Figure 6B, Video 6**)(33, 34). Prolonged OGD caused neuronal swelling and a return to baseline after reperfusion, similar to our previous publication using a $[Cl^-]_i$ biosensor(35). Prolonged and brief OGD caused a robust and significant elevation in the neuronal N/C ratio (**Supplemental Figure 6D, E**). Although brief OGD caused no long-lasting swelling, the elevation of the N/C ratio during reperfusion was significantly larger than that caused by prolonged OGD (**Supplemental Figure 6F**), suggesting that nuclear translocation of macromolecules, like GCaMP, may represent a form of reperfusion injury(36, 37). These data confirm that nuclear translocation of GCaMP is a robust and common phenotype following different forms of pathological neuronal hyperexcitability and can occur independently from neuronal swelling.

NMDA-induced excitotoxicity increases nuclear pore size in neonatal neocortical neurons.

We next evaluated the process of GCaMP6s translocation to the nucleus during excessive neuronal excitation. Bidirectional trafficking across the nuclear envelope of small (20-40 kD) and large molecules

(> 40 kD) occurs through passive diffusion or by receptor-facilitated transport through the nuclear pore complex (NPC), respectively(12, 13). Nuclear transport is regulated by the endoplasmic reticulum and nuclear envelope Ca^{2+} stores and modulated by the neuronal activity(38). Prior studies in cultures and transgenic mice demonstrated the degradation of the nuclear membrane and an increase in NPC size caused by prolonged (several hours to days) exposure to cytotoxic insults(14, 39, 40). We investigated whether an increase in NPC size underlies the nuclear translocation of GCaMP6s following more acute excitotoxic insults reminiscent of seizures or stroke. After confirming NMDA-induced elevation of the N/C ratio using multiphoton imaging, the same Thy1-GCaMP6s slices were post-fixed, resin-embedded, and stained to prepare ultra-thin sections (~70 nm) for transmitted electron microscopy. (**Figure 5A**). The entire neuronal nuclei were imaged at low magnification (~6,000x), followed by high-magnification images of the nuclear envelope containing nuclear pores (~25,000x, **Figure 5B**). The nuclear pore sizes were quantified as the distance between the first and last electron density peaks across a linear ROI spanning the entire pore (**Figure 5C**). We found that the average nuclear pore size increased by ~29% following NMDA treatment (**Figure 5D**), with a significant increase in the total pore size distribution (**Fig .5E**). There was no change in the density of pores per µm, nuclear area, or nuclear perimeter (**Figure 5F-H**) between aCSF and NMDA-treated neurons. Interestingly, nuclear circularity was reduced with NMDA (**Figure 5I**), possibly due to an increase in activity-dependent ER invaginations into the nuclear membrane(41, 42). Therefore, these data suggest that excitotoxicity-induced increase in nuclear pore size and the resulting increase in the nuclear envelope permeability allows the translocation of a large cytoplasmatic protein, in this case, GCaMP6s, into the neuronal nucleus.

Mitigating neuronal swelling during NMDA-mediated excitotoxicity does not prevent the increase in the N/C ratio.

We next asked if the NMDA-mediated increase in neuronal N/C is preventable by mitigating neuronal swelling. Neuronal swelling is primarily mediated by the co-transport of water molecules accompanying

Na^+ and Cl^- influx(35, 43–46). While osmotic agents and surgical treatments mitigate brain swelling in the clinic, the prognoses remain poor for these patients(5–7). The poor clinical outcomes suggest that alternative cellular consequences of excitotoxic injury (e.g., excessive NMDA receptor-mediated Ca^{2+} influx) may contribute to the deleterious effects independent of neuronal swelling. We hypothesized that if the elevated N/C ratio (during excessive NMDAR activation) is independent of neuronal swelling, then mitigating swelling should not prevent the increase in the N/C ratio. To test this, we used hypertonic aCSF (+40 mOsm)(43) as an osmotic agent to mitigate the effects of NMDA-induced neuronal swelling.

First, we tested if osmotic perturbations alone could change neuronal N/C ratios. We treated Thy1-GCaMP6s slices with hypertonic or hypotonic aCSF that induced transient shrinkage or swelling in neonatal neocortical neurons, respectively (**Supplemental Figure 7A**). We found that hypertonic or hypotonic aCSF did not affect the N/C ratio (**Supplemental Figure 7B-C**). Next, we induced NMDA-mediated cytotoxic edema in the presence of hypertonic aCSF (+40 mOsm) to mitigate neuronal swelling. Although we observed neuronal swelling immediately after NMDA application, persistent swelling was decreased by hypertonic aCSF, and neuronal volumes returned to baseline by 40 min (**Figure 6A, B**). The proportion of swollen neurons also decreased in hypertonic aCSF at 40 min (**Figure 6E**). We confirmed the mitigation of NMDA-mediated neuronal swelling and dendritic beading by hypertonic aCSF by imaging YFP-expressing neurons (Thy1-H-YFP mice, **Supplemental Figure 8)**. Critically, hypertonic aCSF did not prevent the NMDA-mediated elevation of neuronal N/C ratios (**Figure 6C, D**). These results suggest that abnormal nuclear translocation and elevated N/C ratios of cytosolic proteins, in this instance measured with GCaMP6s, may represent an early marker of a cytotoxic mechanism occurring during NMDAR-mediated excitotoxicity, independent of neuronal swelling.

*Nuclear translocation of GCaMP6s after NMDA-mediated excitotoxicity is calpain-mediated***.**

Thus far, our data suggest that different excitotoxic insults to the neonatal neocortex cause nuclear translocation of large biomolecules, including GCaMP6s, through increased nuclear envelope

permeability independent of neuronal swelling. Nuclear translocation of GCaMP6s in neurons correlated with elevation of intracellular Ca^{2+}, suggesting a Ca^{2+}-dependent mechanism. Calpains, a family of Ca^{2+} activated cysteine proteases, can play a critical role in mediating the increase in N/C ratio, as they are linked to multiple pathologic conditions, including excitotoxicity and trauma-induced neurodegeneration and cell death(47, 48). Prior studies in neuronal cultures suggest that increased nuclear envelope permeability is associated with the activation of calpains(40). Thus, we wanted to test if the elevation of the N/C ratio that follows NMDA-excitotoxic injury could be prevented by inhibiting calpains in the neonatal neocortex. We incubated Thy1-GCaMP6s slices in a calpain inhibitor (MDL 28170)(49, 50) for at least 30 minutes before multiphoton imaging (**Figure 7A, B**). Surprisingly, MDL pretreatment significantly reduced NMDA-induced neuronal swelling. Moreover, MDL, in the presence of hypertonic aCSF, further mitigated NMDA-induced neuronal swelling (**Figure 7C**). More importantly, MDL prevented NMDA-induced elevation in the N/C ratio compared to vehicle-treated neurons. A similar suppression of N/C elevation was observed with MDL plus hypertonic aCSF (**Figure7D, E**). Next, to confirm these results *in vivo*, we injected neonatal Thy1-GCaMP6s mice (P11-17) with MDL (IP: 30mg/Kg) ~1 hr before craniotomy (**Figure 7F**). We found that blocking calpains with MDL prevented NMDA-mediated neuronal swelling in neonates *in vivo* (at 40 min, **Figure 7G**) and most importantly, MDL prevented the elevation of the N/C ratio compared to vehicle-treated mice (**Figure 7G**), consistent with our *in vitro* results. These results indicate that Ca^{2+}-regulated calpain activation contributes to increased permeability of the nuclear envelope and subsequent nuclear translocation of GCaMP6s following excitotoxic injury in the neonatal brain.

Discussion

We evaluated changes in neuronal swelling and the concurrent translocation of cytosolic GCaMP6s, a fluorescent Ca^{2+} indicator, to the nucleus under various brief insults in neonatal neocortical neurons in acute brain slices and *in vivo*. We observed that different insults induced an elevation in $[Ca^{2+}]_i$ in

neonatal neurons (**Figure 1**), accompanied by a gradual increase in the nuclear GCaMP6s signal, which was quantified as an increase in the N/C ratio (**Figure 2-4**). The increase in the N/C ratio was associated with persistent $[Ca^{2+}]_i$ elevation and could occur independently of swelling (**Figure 4, Supplemental Figure 6-7**). The nuclear entry of GCaMP6s due to excitotoxic injury correlated with larger nuclear pore sizes (**Figure 5**). Critically, mitigating excitotoxic edema using hyperosmotic conditions did not normalize the elevated N/C ratio (**Figure 6**). Yet, the elevation was prevented by inhibiting calpains (**Figure 7**). Thus, our data demonstrated that even preventing neuronal swelling during brain injury does not prevent abnormal translocation of sizeable cytoplasmic proteins (GCaMP6s) and could be a cause for the poor outcomes of patients undergoing treatment for brain swelling(5, 6). Also, our data suggest that the N/C ratio can be used as an early biomarker of injured neurons.

In our experiments, multiple hyperexcitability or excitotoxicity-inducing insults independently caused nuclear translocation of cytosolic GCaMP6s in a subset of neonatal neocortical neurons. GCaMPs are among the most widely used Ca^{2+} indicators due to their high sensitivity to Ca^{2+}, good signal-to-noise ratio, and rapid response kinetics(9, 10). Although their expression is restricted to the cytosol, reports suggest that GCaMPs can translocate to nuclei in certain neurons, but the mechanism or timing is unclear. Neurons with abnormal GCaMP nuclear accumulation often show altered Ca^{2+} dynamics and intrinsic excitability (e.g., increased firing rates)(11, 17, 18). Thus, the abnormal accumulation of nuclear GCaMP could be a marker of cytotoxicity or death as the degradation of the nuclear pore complex, which increases the leakiness of the nuclear barrier, is often observed in apoptotic or injured neurons(14, 15, 39). Unfortunately, many studies discard these neurons as “unhealthy cells” from their analysis. Abnormal nuclear accumulation of virally-delivered GCaMP6s and a resultant elevation in nuclear to cytosolic fluorescence ratio has been described in cultured cortical neurons in a few weeks after viral infection(11). In contrast, we showed real-time nuclear translocation of GCaMP6s in neonatal neurons in response to brief neuronal excitotoxicity within minutes, quantified as nuclear: cytosolic intensity ratio (N/C). The abnormal nuclear translocation of GCaMP6s occurred following various

excitotoxic insults in acute brain slices, post-fixed tissue, and in *vivo* multiphoton imaging in neonatal mice, confirming the robustness of our findings. Since GCaMPs are widely used by the neuroscience community to determine neuronal activity in experimental models of brain injury, neurodegeneration, and hyperexcitability, an increase in the N/C ratio could also be used as an early indicator of cytotoxic consequences.

The elevation of the N/C ratio was associated with an increase in the size of neuronal nuclear pores (**Figure 5**), suggesting altered nuclear macromolecular transport, perhaps causing dysregulation of nuclear function. Our data supports prior evidence from cultures that neuronal cytotoxic injury increases nuclear envelope permeability, resulting in the transport of cytosolically localized macromolecules into the nucleus(15, 51). The nuclear pore complexes (NPCs) mediate bidirectional transport between the cytoplasm and the nucleus. The pores form a size-selective 'molecular sieve,' restricting the passive diffusion of proteins larger than 40 kDa(12, 52). Larger molecules move across the nuclear envelope through a transport receptor-facilitated translocation(13, 38). Abnormally elevated cytoplasmatic Ca^{2+} levels following prolonged activation of NMDARs can massively impair nuclear transport and disrupt multiple cellular functions(53). Moreover, excessive Ca^{2+} influx following prolonged NMDAR activation can lead to calpain-mediated degradation of NPC components, increasing the nuclear membrane permeability(16, 40, 54). Additionally, Ca^{2+} is a potent regulator of gene expression, and nuclear Ca^{2+} signaling, in response to various stimuli, can facilitate or suppress gene transcription(55–57), including cell death pathways (e.g., Caspase3 or MLKL)(58) or the suppression of transcription-dependent neuroprotective pathways (e.g., CREB/BDNF)(59, 60).

Most of the experimental evidence supporting excitotoxic damage to NPCs has been done in neuronal cultures or non-neuronal cells. It is relatively unknown whether excitotoxicity alters neuronal nuclear dynamics in neonates. Our study is the first to show, *in vivo* and *ex vivo,* that brief excitotoxic insults cause an increase in neuronal nuclear pore size independent of neuronal swelling. We speculate that

the elevated N/C ratio observed in a subgroup of neurons exposed to an intense activation (hypoxia, seizures, repeated stimulation) is an early marker of neuronal injury. Further work is needed to correlate the N/C ratio to injury markers and to understand how it is that not all neurons exposed to cytotoxic damage have an elevated N/C ratio.

Inhibiting calpains prevented NMDAR-mediated nuclear translocation of GCaMP6s, both *in* and *ex vivo* (**Figure 7**). Calpains are a family of calcium-dependent proteases with two major isoforms in the brain (calpain 1 and 2, also called μ- and m-calpain, respectively). Both isoforms are activated by elevated $[Ca^{2+}]_i$ following intense neuronal stimulation(47, 61). While both isoforms share a variety of substrates, their physiological roles can often be contradictory. Calpain-1 activation downstream of synaptic NMDARs promotes long-term hippocampal potentiation (LTP), while calpain-2 activation via extrasynaptic NMDARs can hamper synaptic potentiation and contributes to neurodegeneration(62–64). However, their regulatory role in cell death is complementary, with both isoforms affecting a wide array of substrates that mediate necrotic, apoptotic, and autophagic cell death(48, 65–67). Moreover, multiple studies have implicated calpains in the degradation of nuclear membranes during cell death or following intense and prolonged NMDAR activation(14, 16, 40, 54). Our data support these previous findings and strongly suggest that calpain-mediated degradation of the nuclear pore underlies GCaMP6s translocation into the nucleus, following various and even brief brain insults.

The current dogma recognizes cytotoxic neuronal swelling and resulting cell death as one of the leading causes of morbidity in conditions associated with severe brain edema(44, 45). Yet, using osmotic agents and surgical interventions to mitigate brain swelling continue to yield poor clinical outcomes(5, 6). Swelling after intense neural activity often depends on the influx of Na^+ predominantly through voltage-gated channels and glutamate receptors and Cl^- influx through various channels and transport mechanisms(35, 45, 46). Since neurons do not express water-permeant aquaporins, water accumulates using ionic transport through different pathways, including the cation-chloride cotransporters(35,

68). Cl^- and other ions can accumulate in neurons following intense activity, which can induce ionic overload and, in turn, alter synaptic responses and worsen neuronal intrinsic excitability(22, 69–72), leading to further swelling. However, neuronal swelling might not always cause cell death. Homeostatic regulatory responses can normalize the neuronal volume and ionic gradients in response to pathogenic cell swelling or shrinkage, limiting the impact that neuronal swelling may have on eventual cytotoxic injury(73–75). This homeostatic neuronal volume regulation is present in neonates during brief OGD(35) and replicated in this study and during hypo- or hyperosmotic conditions (**Supplemental Figure 7**). Also, not all neurons swell or return to baseline after volume changes(35) (**Supplemental Figure 7,8**). However, we report a novel, calpain-mediated mechanism of abnormal nuclear translocation of macromolecules independent of swelling as an early expression of neuronal injury. We speculate that this swelling-independent mechanism of neuronal injury can begin to explain why even with adequate control of brain edema, including surgical decompression, there is no significant morbidity improvements(5, 6). This clinical observation is supported by our findings that hypertonic saline improved neuronal swelling but did not decrease the N/C ratio. Significantly, blocking calpains prevented an elevation of the N/C ratio *in* and *ex vivo* and decreased neuronal swelling, suggesting that blocking calpains may also aid in treating neuronal swelling.

In conclusion, we observed that multiple brief injuries to neonatal neocortical neurons caused a calpain-dependent increase in the permeability of the NPCs, resulting in the translocation of GCaMP6s from the cytoplasm into the nucleus. This phenomenon was independent of the neuronal swelling in the neonatal period. These findings could explain the poor clinical outcomes even when the clinical treatment of brain edema is nominally adequate and suggest that elevation of the N/C ratio may be a valuable biomarker of early neuronal injury.

Methods

Study approval

All experiments were conducted in accordance with a protocol approved by the Institutional Animal Care and Use Committee of the University of Iowa.

Animals

We used transgenic mice expressing a genetically encoded calcium indicator, GCaMP6s, under the *Thy1* promoter. For *in vitro* explements, brain slices were prepared using postnatal days 8 to 12 (P8-12) hemizygous and homozygous male and female Thy1GCaMP6s mouse pups. *In vivo* imaging experiments were performed on slightly older (P12-17) pups under anesthesia. There was no observable difference in post-NMDA neuronal swelling and nuclear translocation of GCaMP6s between male and female Thy1-GCaMP6s mice pups. Transmission electron microscopy (TEM) experiments used four slices (P11, 2 NMDA, 2 aCSF control). Immunohistochemistry (IHC) was performed on 12 brain slices from three P8-12 pups (two male, one female). For dual-color imaging experiments, we used WT (C57B/l6, Jaxlab# 000664) P1-2 pups injected intraventricularly with a viral vector to express GCaMP6s and mRuby2 (Addgene# pAAV-hSyn1-mRuby2-GSG-P2A-GCaMP6s) The injected pups recovered, and they were in good health on the day of the experiment. All animals were housed in a temperature and humidity-controlled vivarium with free access to food and water on a 12-hour light/dark cycle.

Intraventricular (ICV) Viral injections

ICV viral injections were conducted on neonatal C57BL/6 pups (P1-2). Co-expression of GCaMP6s and mRuby2 in neocortical and hippocampal neurons was achieved by injecting pAAV-hSyn1-mRuby2-GSG-P2A-GCaMP6s one week before imaging (**Figure1A**; Addgene, catalog # 50942-AAV1; 1.2×10^{13} GC/mL). Animals were anesthetized using hypothermia. The anesthetized pup's head was sterilized with a cotton swab soaked in 70% ethanol. Two µl of the virus plus 0.05% trypan blue was slowly injected into the brain (0.8-1 mm lateral from the sagittal suture, halfway between lambda and bregma) to a depth of ~3 mm using a glass micropipette. After the injection, pups were marked using a pen,

allowed to recover on a heating pad, and returned to their home cage. The injected pups were visually inspected for signs of pain or distress post-surgery and were euthanized if they were found in distress.

Preparation of acute brain slices

Male and female mouse pups were anesthetized using isoflurane inhalation and decapitated per a protocol approved by the Institutional Animal Care and Use Committee of the University of Iowa. Each brain was removed and placed in ice-cold artificial cerebrospinal fluid (aCSF) containing (in mM) NaCl (116), KCl (3.3), $CaCl_2$ (1.3), NaH_2PO_4 (1.25), $NaHCO_3$ (25), and D-glucose (10) and mannitol (20) along with a high $MgCl_2$ concentration (2) and kynurenic acid (2) to block glutamatergic receptors (Osmolarity: 300 mOsm). The aCSF was saturated with carbogen (95% O_2 and 5% CO_2) to maintain a pH of 7.3 - 7.4. Thick coronal sections (450 µm) containing the sensory neocortex and hippocampus were cut using a vibratome (Leica VT1000S) while submerged in aCSF. The brain slices were then placed in an interface holding chamber containing aCSF used for physiological recordings, devoid of kynurenic acid and with 1.3 mM $MgCl_2$, at room temperature for 30 min. Afterward, the temperature was slowly increased to and maintained at 30 °C. Slices were incubated for at least one hour before being transferred to the recording chamber.

Surgery for awake imaging

Surgical window implantation for *in vivo* imaging was performed on the day of recording at P12-17 Thy1GCaMP6s pups. Anesthesia was induced with 5% isoflurane inhalation using the SomnoSuite delivery system (Kent Scientific Corporation). Pups were mounted on a stereotactic assembly with a nose-cone mask suitable for neonates. A circular craniotomy (~5 mm diameter) over the sensory neocortex was done using a dental drill. When removing the skull, measures were taken to reduce damage to the dura and underlying cortex (76). The brain was hydrated with saline or saline-soaked surgical foam. A barrier was built around the craniotomy using cyanoacrylate glue and dental cement (Stoelting

#51458 & 51456) to retain saline over the exposed brain. The pups and the stereotaxic frame were transferred to a stage for *in vivo* two-photon imaging.

In vitro multiphoton imaging

Slices were placed in a submerged chamber constantly perfused with recording aCSF maintained at 30 °C. The location of the sensory neocortex was determined using epifluorescence. *In vitro* two-photon laser scanning microscopy (2PLSM) was performed using the Bruker Ultima galvo-resonant system mounted on an Olympus BX51WIF upright microscope body with a water immersion objective (20X, 1.0 N.A.). A single Ti: sapphire tunable laser (Mai Tai HPDS; Spectra-Physics) generated two-photon excitation (920 nm) for both GCaMP6s and mRuby2. Scanning was performed with galvo-mirrors. Emitted light was bandpass filtered at 565 nm using a dichroic mirror (T510lpxrxt, Chroma), and green and red emission wavelengths were isolated using specific filters: 525/35 nm (green) and 595/25 nm (red). Two GaAsP or multi-alkali photomultiplier tubes (PMT, Hamamatsu Photonics) were used to simultaneously acquire green and red signals. Images were acquired in Layer IV/V of the sensory neocortex. Three-dimensional stacks (3D) of raster scans in the XY plane were imaged at 2 µm intervals with a 512×512-pixel resolution. Time series acquisition of single XY planar raster scans was performed at a 256x256-pixel resolution at 2.67 frames/second. All images were acquired at 2X digital zoom. Some sections were post-fixed after 2PLSM for further analysis by IHC or TEM (see below).

In vivo multiphoton imaging

Pups were maintained under inhaled isoflurane anesthesia (2.5-3.5%) during the imaging session. We used a Bruker-Ultima resonant-galvo system with an identical configuration to the *in vitro* system. *In vivo,* imaging through the craniotomy was performed using a Nikon LWD water immersion objective (16X, 0.8 N.A.). Two-photon images were acquired using galvo-scanning at a minimum depth of 200 µm from the surface. GCaMP6s was excited at a wavelength of 920 mm, and emission was filtered and

acquired using a single GaAsP PMT (Hamamatsu Photonics). Time series acquisition of single XY planar raster scans was performed at a 256x256-pixel resolution at ~2.67 frames/second speed. Movement in XY dimensions was minimal and was corrected by motion correction algorithms (ImageJ). Motion artifact in the Z plane was identified by frames with repeated cytoarchitecture. All images were acquired at 2X digital zoom.

Pharmacological interventions and excitotoxic perturbations.

See the Key Resources Table for a detailed description of pharmacological agents and other chemicals used in this study. Stock solutions were prepared for all compounds in dimethyl sulfoxide (DMSO; Sigma-Aldrich # 472301) or regular aCSF depending on their solubility. The stocks were then diluted into aCSF (*in vitro*). NMDA (30 µM, 10 mins) was applied to induce excitotoxic injury in slices. 4-AP (100 µM, ~70 mins.) was used to generate seizure-like activity. Hypertonic (+40 mOsm) and hypotonic (-20 mOsm) conditions were created by adding or removing 20 mM mannitol to the regular aCSF. Whenever appropriate, vehicles contained identical DMSO concentrations to respective stock solutions of the drugs (all ≤ 1%). All drugs were perfused *in vitro* at 2 mL/min and took <30 seconds to reach the recording chamber. For *in vivo* experiments, MDL stock (3.8 mg/mL) was prepared in a vehicle containing 50% saline and 50% DMSO. The amount of stock (or vehicle) corresponding to the dose (30mg/kg) was intraperitoneally injected in mice for at least 1 hour before the experiment. The total volume injected was always less than 80 µl.

Repeated micro-stimulation using focal NMDA puffs.

Pulled glass micropipettes (0.5–1 MΩ resistance, tip size 10–20 µm) were filled with 100 mM NMDA and placed on the neocortical surface of acute brain slices. NMDA was applied as brief puffs (3psi, 100 ms) using a pressure ejector (MPPI-2, Applied Scientific Instruments). Each stimulus consisted of three brief NMDA puffs, separated by 2 seconds. Every stimulus resulted in a Ca^{2+} transient.

Immunohistochemistry (IHC)

After *in vitro* imaging or incubation, slices were fixed with 4% PFA in PBS at 4°C overnight. The fixed slices were then washed with PBS, dehydrated in 30% sucrose (4°C overnight), and either embedded in blocks of 15% porcine gelatin (type A) or cryopreserved in a solution containing 40% PBS, 35% ethylene glycol, and 25% glycerol. The brain blocks were cut coronally (10 µm) using a cryostat (CM3050S, Leica). Sections were permeabilized with 0.2% Triton X-100 in PBS for 30 min at room temperature. Sections were mounted on slides using a media containing 4,6-diamidino-2-phenylindole (DAPI) to visualize cellular nuclei. Slides were imaged under a 10x objective on an epifluorescence microscope (Leica SPE confocal microscope) using the following filters: blue: ex360/40, em470/40, dc400; green: ex480/40, em527/30, dc505. We used a blue filter for DAPI and green for GCaMP6s. The entire section was imaged using the Leica Application Suite X program. All images from an experimental set were recorded at 12 bits (2.20 pixels/µm) using identical fluorophore exposure times and gain for each slide. Image J was used to analyze the images. The analysis was conducted in the somatosensory region of the neocortex (average area = 1.10 mm^2). ROIs were drawn manually for GCaMP6s.

Transmission Electron Microscopy (TEM)

After 2PLSM, live coronal sections were fixed in a solution containing 2% paraformaldehyde and 2% glutaraldehyde in 0.1 M Sodium Cacodylate buffer, pH 7.4. The sections were then post-fixed with 1% osmium tetroxide aqueous solution containing 1.6 % ferrocyanide and contrasted with 2.5% uranyl acetate aqueous solution. After dehydration in a graded ethanol series up to 100% and immersion in propylene oxide, sections were infiltrated with Eponate 12 resin (Ted Pella Inc, Cat#18010) and then flat-embedded between Aclar films (Ted Pella Inc, Cat# 10501) with Eponate resin, and polymerized overnight at +60°C. Chips with L4 and 5 of the sensory neocortex were selected by light-microscopic inspection, glued to blank epoxy blocks, and sectioned with an ultramicrotome (Leica microsystems).

Ultrathin sections (~70 nm) were collected, mounted on 200 mesh copper grids, and stained with 5% uranyl acetate and Reynold's lead citrate solutions. Contrasted grids were examined with an HT7800 Transmission electron microscope. Before the acquisition, L5 neurons were identified in real-time using a low-resolution CCD camera (Hitachi), and images were acquired with an AMT Nanosprint 15 digital, high-sensitivity camera system with a 5056 x 2960-pixel sensor. Low-magnification images of the whole nuclei (5 or 6,000x) and high-magnification images of the nuclear membrane segments (25,000x or more) were captured.

In vitro extracellular electrophysiology

Acute brain slices were placed in an interface chamber (32–34°C) and perfused with aCSF saturated with 95% O_2 and 5% CO_2. Glass electrodes filled with aCSF were placed in the neocortex (layers IV and V of somatosensory regions) identified using a stereomicroscope (AmScope). Extracellular field potentials were recorded using a low-noise differential amplifier (DP-311, Warner Instruments, 100x gain) and digitized at 2 kHz (IX/408, iWorx Systems Incorporated). NMDA was briefly applied to the slices (30µM, 10 minutes) to induce an acute excitotoxic injury. Field potentials at baseline, during NMDA treatment, and washout were analyzed using a custom-written macro in IgorPro v8.04 (Wave-Metrics).

Measuring neuronal areas and intracellular Ca^{2+} levels

Z-stacks acquired using 2PLSM were background-subtracted, smoothened (median filter, radius=2), converted to maximum intensity projections (MIPs, every 10 images), and contrast-enhanced (CLAHE, ImageJ). Thus, the maximal areas for each neuron over a 20 µm depth were represented in a MIP (68). Neuronal cell bodies in the processed MIPs were detected using an automated neuronal morphology analysis framework (ANMAF) based on a convolutional neuronal network (21) and saved as regions of interest (ROIs) for further analysis. For images acquired in dual color, neuronal ROI sets were

generated separately for each channel (GCaMP6s and mRuby2) using ANMAF. A custom-built macro automatically updated neuronal ROIs to the z-planes corresponding to the maximum area. Change in intracellular $[Ca^{2+}]_i$ was measured as the ratio of median GCaMP6s and mRuby2 intensities (Green/Red ratio) for each neuronal ROI.

Measuring the nuclear/cytosolic fluorescence ratio (N/C ratio)

Traditional GECIs like GCaMP6s have cytosolic localization, with most of the signal emerging from the cytosol and nuclei appearing darker in comparison. Using neuronal ROIs generated by ANMAF, we confirmed the presence of nuclei in their respective z-planes. Then using a custom-built, automated macro, circular ROIs (15 µm in diameter) were drawn at the center of mass of all the neuronal ROIs (hereafter called nuclear ROIs), and their XY locations were adjusted (if needed). The nuclear ROIs were then subtracted from the ANMAF-generated neuronal ROIs (using the XOR function) to generate the cytosolic ROI. The ratio of mean intensities of nuclear and cytosolic ROIs was calculated for every neuron at the corresponding z-plane.

Measurement of neuronal Ca^{2+} transients

Image processing, demarcation of regions of interest (ROI), and collection of fluorescence traces were performed in Fiji using proprietary and custom-built macros. Fluorescence traces were analyzed in IgorPro8 (Wavemetrics) and Prism 9 (GraphPad). Raw images in time series were background-subtracted, smoothened (median filter, radius=2), and compressed into maximum intensity projections (MIPs). Circular ROIs representing neuronal somas and concentric, doughnut-shaped ROIs representing the neuropil were generated on the MIPs using a semi-automated, custom-built macro. The neuropil fluorescence was subtracted from the corresponding somatic fluorescence for each frame. To determine the characteristics of evoked Ca^{2+} responses, we performed baseline subtraction and normalization ($\Delta F/F_0$) of the neuropil-subtracted Ca^{2+} signal for each neuron using the following equation:

$(F_t-F_0)/F_0$, where F_t is the fluorescence intensity of a given frame, and F_0 is the average fluorescence of the first 8-10s of the trial (before micro-stimulation *in vitro* using NMDA puffs). To determine the characteristics of spontaneous Ca^{2+} transients, the neuropil-subtracted traces of neuronal fluorescence were transformed into Z-scores using the following equation: $Z = (F_t-F_M)/\sigma$, where F_t is the fluorescence intensity of a given frame, F_M is the average fluorescence of the entire trace, and σ is the standard deviation of the fluorescence for the whole trace.

Statistics

The data were acquired at multiple time points (0' or baseline, 10' or after NMDA, 20', 30', 40' or wash-out). A subset of ANMAF-generated neuronal ROIs was matched in multiple time points using a custom-built macro (Igor 8). The normality of distributions was determined using the D'Agostino–Pearson K2 and Anderson-Darling tests. Data are presented as mean ± confidence interval (95% CI) or median ± interquartile range (IQR) based on normality distribution. As a functional correlate of intracellular Ca^{2+}, ratios of median intensities of green and red channels were calculated for every neuronal ROI (Green/Red ratios) and represented as mean ± 95% CI. Matched data representing multiple time points with the same perturbation were analyzed using repeated measures one-way ANOVA with Dunnett's test for multiple comparisons (Friedman's test with Dunn's multiple comparison tests for non-parametric data). Unpaired parametric data across multiple time points were analyzed using one-way ANOVA (or Kruskal-Wallis test for non-parametric data). Data with multiple time points were compared across groups using two-way ANOVA with Tukey's test for multiple comparisons. Data points representing individual slices/cells were compared across groups using a two-tailed, unpaired t-test (parametric data) or Mann–Whitney U test (non-parametric data). Paired comparisons were performed using a two-tailed, paired t-test. Normalized (%) distributions of individual events were compared across genotypes using a two-sample Kolmogorov–Smirnov (KS) test. Statistical significance was considered at $p<0.05$.

Data availability

The datasets and code used for image processing and data analysis in the current study have not been deposited in a public repository but are available on request. This study did not use nor generate any new, unique reagents. Requests for resources and reagents should be directed to and will be fulfilled by the corresponding author, Dr. Joseph Glykys (joseph-glykys@uiowa.edu).

Author contributions

P.S. and J.G. designed the study and wrote the manuscript. P.S. and R.L. designed and performed experiments. P.S., R.L., and K.F. processed and analyzed data. J.G. provided technical direction and supervision.

Acknowledgment

We thank Jax Labs and Dr. Douglas Kim (HHMI) for the Thy1-GCaMP6s mice, and Dr. Joshua Sanes (Harvard University) for the Thy1-H-eYFP mice. pAAV-hSyn1-mRuby2-GSG-P2A-GCaMP6s-WPRE-pA was a gift from Drs. Tobias Bonhoeffer, Mark Huebener, and Tobias Rose. We sincerely thank Chantal Allamargot and the Central Microscopy Research Facility (CMRF) at the University of Iowa for their help with transmission electron microscopy. JG was funded by NIH/NINDS R01NS115800 and the Iowa Neuroscience Institute. This research was partly supported by the computational resources provided by the University of Iowa, Iowa City, Iowa, and The University of Iowa Hawkeye Intellectual and Developmental Disabilities Research Center (HAWK-IDDRC) P50 HD103556.

.

References

1. Unterberg AW, Stover J, Kress B, Kiening KL. Edema and brain trauma. *Neuroscience* 2004;129(4):1019–1027.

2. Battey TWK et al. Brain Edema Predicts Outcome After Nonlacunar Ischemic Stroke. *Stroke* 2014;45(12):3643–3648.

3. Stokum JA, Gerzanich V, Simard JM. Molecular pathophysiology of cerebral edema. *J Cereb Blood Flow Metab* 2016;36(3):513–538.

4. Cooper DJ et al. Decompressive Craniectomy in Diffuse Traumatic Brain Injury. *New England Journal of Medicine* 2011;364(16):1493–1502.

5. Hutchinson PJ et al. Trial of Decompressive Craniectomy for Traumatic Intracranial Hypertension. *New England Journal of Medicine* 2016;375(12):1119–1130.

6. Kolias AG et al. Evaluation of Outcomes Among Patients With Traumatic Intracranial Hypertension Treated With Decompressive Craniectomy vs Standard Medical Care at 24 Months: A Secondary Analysis of the RESCUEicp Randomized Clinical Trial. *JAMA Neurology* 2022;79(7):664–671.

7. Ferrari DC, Nesic O, Perez-Polo JR. Perspectives on Neonatal Hypoxia/Ischemia-Induced Edema Formation. *Neurochem Res* 2010;35(12):1957–1965.

8. Berridge MJ, Bootman MD, Roderick HL. Calcium signalling: dynamics, homeostasis and remodelling. *Nat Rev Mol Cell Biol* 2003;4(7):517–529.

9. Akerboom J et al. Optimization of a GCaMP Calcium Indicator for Neural Activity Imaging. *J. Neurosci.* 2012;32(40):13819–13840.

10. Chen Q et al. Imaging Neural Activity Using Thy1-GCaMP Transgenic mice. *Neuron* 2012;76(2):297–308.

11. Yang Y et al. Improved calcium sensor GCaMP-X overcomes the calcium channel perturbations induced by the calmodulin in GCaMP. *Nat Commun* 2018;9(1):1504.

12. Miao L, Schulten K. Transport-Related Structures and Processes of the Nuclear Pore Complex Studied Through Molecular Dynamics. *Structure* 2009;17(3):449–459.

13. Wente SR, Rout MP. The Nuclear Pore Complex and Nuclear Transport. *Cold Spring Harb Perspect Biol* 2010;2(10):a000562.

14. Bano D et al. Alteration of the nuclear pore complex in Ca2+-mediated cell death. *Cell Death Differ* 2010;17(1):119–133.

15. Strasser C, Grote P, Schäuble K, Ganz M, Ferrando-May E. Regulation of nuclear envelope permeability in cell death and survival. *Nucleus* 2012;3(6):540–551.

16. Yamashita T, Aizawa H, Teramoto S, Akamatsu M, Kwak S. Calpain-dependent disruption of nucleo-cytoplasmic transport in ALS motor neurons. *Sci Rep* 2017;7(1):39994.

17. Tian L et al. Imaging neural activity in worms, flies and mice with improved GCaMP calcium indicators. *Nat Methods* 2009;6(12):875–881.

18. Resendez SL et al. Visualization of cortical, subcortical and deep brain neural circuit dynamics during naturalistic mammalian behavior with head-mounted microscopes and chronically implanted lenses. *Nat Protoc* 2016;11(3):566–597.

19. Rose T, Jaepel J, Hübener M, Bonhoeffer T. Cell-specific restoration of stimulus preference after monocular deprivation in the visual cortex. *Science* 2016;352(6291):1319–1322.

20. Glascock JJ et al. Delivery of Therapeutic Agents Through Intracerebroventricular (ICV) and Intravenous (IV) Injection in Mice. *J Vis Exp* 2011;(56):2968.

21. Tong L, Langton R, Glykys J, Baek S. ANMAF: an automated neuronal morphology analysis framework using convolutional neural networks. *Sci Rep* 2021;11(1):8179.

22. Dzhala V, Valeeva G, Glykys J, Khazipov R, Staley K. Traumatic Alterations in GABA Signaling Disrupt Hippocampal Network Activity in the Developing Brain. *J. Neurosci.* 2012;32(12):4017–4031.

23. Akam T, Walton ME. pyPhotometry: Open source Python based hardware and software for fiber photometry data acquisition. *Sci Rep* 2019;9(1):3521.

24. Peng X, Huang X, Du K, Liu H, Chen L. High spatiotemporal resolution and low photo-toxicity fluorescence imaging in live cells and in vivo. *Biochemical Society Transactions* 2019;47(6):1635–1650.

25. Rothman SM, Olney JW. Excitotoxity and the NMDA receptor. *Trends in Neurosciences* 1987;10(7):299–302.

26. Pietrobon D, Moskowitz MA. Chaos and commotion in the wake of cortical spreading depression and spreading depolarizations. *Nat. Rev. Neurosci.* 2014;15(6):379–393.

27. Zeiler FA, Teitelbaum J, Gillman LM, West M. NMDA Antagonists for Refractory Seizures. *Neurocrit Care* 2014;20(3):502–513.

28. Zhou X, Hollern D, Liao J, Andrechek E, Wang H. NMDA receptor-mediated excitotoxicity depends on the coactivation of synaptic and extrasynaptic receptors. *Cell Death Dis* 2013;4(3):e560–e560.

29. Fricker M, Tolkovsky AM, Borutaite V, Coleman M, Brown GC. Neuronal Cell Death. *Physiol Rev* 2018;98(2):813–880.

30. Sadasivan S et al. Acute NMDA toxicity in cultured rat cerebellar granule neurons is accompanied by autophagy induction and late onset autophagic cell death phenotype. *BMC Neurosci* 2010;11:21.

31. Weber M, Taylor C. Damage from oxygen and glucose deprivation in hippocampal slices is prevented by tetrodotoxin, lidocaine and phenytoin without blockade of action potentials. *Brain Research* 1994;664(1–2):167–177.

32. Hartings JA et al. The continuum of spreading depolarizations in acute cortical lesion development: Examining Leão's legacy. *J Cereb Blood Flow Metab* 2017;37(5):1571–1594.

33. Anderson TR, Jarvis CR, Biedermann AJ, Molnar C, Andrew RD. Blocking the Anoxic Depolarization Protects Without Functional Compromise Following Simulated Stroke in Cortical Brain Slices. *Journal of Neurophysiology* 2005;93(2):963–979.

34. Juzekaeva E, Gainutdinov A, Mukhtarov M, Khazipov R. Reappraisal of anoxic spreading depolarization as a terminal event during oxygen–glucose deprivation in brain slices in vitro. *Sci Rep* 2020;10(1):18970.

35. Takezawa Y et al. Role of NKCC1 and KCC2 during hypoxia-induced neuronal swelling in the neonatal neocortex. *Neurobiology of Disease* 2023;178:106013.

36. Fellman V, Raivio KO. Reperfusion Injury as the Mechanism of Brain Damage after Perinatal Asphyxia. *Pediatr Res* 1997;41(5):599–606.

37. Ryou M, Mallet RT. An In Vitro Oxygen–Glucose Deprivation Model for Studying Ischemia–Reperfusion Injury of Neuronal Cells [Internet]. In: Tharakan B ed. *Traumatic and Ischemic Injury: Methods and Protocols*. New York, NY: Springer; 2018:229–235

38. Sarma A, Yang W. Calcium regulation of nucleocytoplasmic transport. *Protein Cell* 2011;2(4):291–302.

39. Faleiro L, Lazebnik Y. Caspases Disrupt the Nuclear-Cytoplasmic Barrier. *Journal of Cell Biology* 2000;151(5):951–960.

40. Sugiyama K et al. Calpain-Dependent Degradation of Nucleoporins Contributes to Motor Neuron Death in a Mouse Model of Chronic Excitotoxicity. *J Neurosci* 2017;37(36):8830–8844.

41. Oliveira AG, Guimarães ES, Andrade LM, Menezes GB, Fatima Leite M. Decoding Calcium Signaling Across the Nucleus. *Physiology (Bethesda)* 2014;29(5):361–368.

42. Mozolewski P et al. The role of nuclear Ca2+ in maintaining neuronal homeostasis and brain health. *J Cell Sci* 2021;134(8):jcs254904.

43. Andrew RD, Lobinowich ME, Osehobo EP. Evidence against Volume Regulation by Cortical Brain Cells during Acute Osmotic Stress. *Experimental Neurology* 1997;143(2):300–312.

44. Liang D, Bhatta S, Gerzanich V, Simard JM. Cytotoxic edema: mechanisms of pathological cell swelling. *Neurosurg Focus* 2007;22(5):E2.

45. Rungta RL et al. The cellular mechanisms of neuronal swelling underlying cytotoxic edema. *Cell* 2015;161(3):610–621.

46. Dzhala V, Egawa K, Kahle KT, Delpire E, Staley K. Chloride Dysregulation, Seizures, and Cerebral Edema: A Relationship with Therapeutic Potential. *Trends in Neurosciences* 2017;40(5):276–294.

47. Bevers MB, Neumar RW. Mechanistic Role of Calpains in Postischemic Neurodegeneration. *J Cereb Blood Flow Metab* 2008;28(4):655–673.

48. Cheng S, Wang S, Lei M, Wang Z, Xiong K. Regulatory role of calpain in neuronal death. *Neural Regen Res* 2018;13(3):556.

49. Thompson SN, Carrico KM, Mustafa AG, Bains M, Hall ED. A Pharmacological Analysis of the Neuroprotective Efficacy of the Brain- and Cell-Permeable Calpain Inhibitor MDL-28170 in the Mouse Controlled Cortical Impact Traumatic Brain Injury Model. *J Neurotrauma* 2010;27(12):2233–2243.

50. Üçeyler N, Biko L, Sommer C. MDL-28170 Has No Analgesic Effect on CCI Induced Neuropathic Pain in Mice. *Molecules* 2010;15(5):3038–3047.

51. Ferrando-May E et al. Caspases mediate nucleoporin cleavage, but not early redistribution of nuclear transport factors and modulation of nuclear permeability in apoptosis. *Cell Death Differ* 2001;8(5):495–505.

52. Corbett AH, Silver PA. Nucleocytoplasmic transport of macromolecules.. *Microbiol Mol Biol Rev* 1997;61(2):193–211.

53. Szydlowska K, Tymianski M. Calcium, ischemia and excitotoxicity. *Cell Calcium* 2010;47(2):122–129.

54. Norberg E et al. An increase in intracellular Ca2+ is required for the activation of mitochondrial calpain to release AIF during cell death. *Cell Death Differ* 2008;15(12):1857–1864.

55. Limbäck-Stokin K, Korzus E, Nagaoka-Yasuda R, Mayford M. Nuclear Calcium/Calmodulin Regulates Memory Consolidation. *J. Neurosci.* 2004;24(48):10858–10867.

56. Papadia S, Stevenson P, Hardingham NR, Bading H, Hardingham GE. Nuclear Ca2+ and the cAMP response element-binding protein family mediate a late phase of activity-dependent neuroprotection. *J Neurosci* 2005;25(17):4279–4287.

57. Bading H. Nuclear calcium signalling in the regulation of brain function. *Nat Rev Neurosci* 2013;14(9):593–608.

58. Zhang S-J et al. Decoding NMDA receptor signaling: identification of genomic programs specifying neuronal survival and death. *Neuron* 2007;53(4):549–562.

59. Hardingham GE, Chawla S, Johnson CM, Bading H. Distinct functions of nuclear and cytoplasmic calcium in the control of gene expression. *Nature* 1997;385(6613):260–265.

60. Hardingham GE, Bading H. Coupling of extrasynaptic NMDA receptors to a CREB shut-off pathway is developmentally regulated. *Biochim Biophys Acta* 2002;1600(1–2):148–153.

61. Metwally E, Zhao G, Zhang YQ. The calcium-dependent protease calpain in neuronal remodeling and neurodegeneration. *Trends Neurosci* 2021;44(9):741–752.

62. Xu J et al. Extrasynaptic NMDA receptors couple preferentially to excitotoxicity via calpain-mediated cleavage of STEP. *J Neurosci* 2009;29(29):9330–9343.

63. Wang Y, Briz V, Chishti A, Bi X, Baudry M. Distinct Roles for μ-Calpain and m-Calpain in Synaptic NMDAR-Mediated Neuroprotection and Extrasynaptic NMDAR-Mediated Neurodegeneration. *J Neurosci* 2013;33(48):18880–18892.

64. Baudry M, Bi X. Calpain-1 and calpain-2: the yin and yang of synaptic plasticity and neurodegeneration. *Trends Neurosci* 2016;39(4):235–245.

65. Williams A et al. Novel targets for Huntington's disease in an mTOR-independent autophagy pathway. *Nat Chem Biol* 2008;4(5):295–305.

66. Ozaki T et al. Inhibitory Peptide of Mitochondrial μ-Calpain Protects against Photoreceptor Degeneration in Rhodopsin Transgenic S334ter and P23H Rats. *PLOS ONE* 2013;8(8):e71650.

67. Müller GJ, Hasseldam H, Rasmussen RS, Johansen FF. Dexamethasone enhances necrosis-like neuronal death in ischemic rat hippocampus involving μ-calpain activation. *Exp Neurol* 2014;261:711–719.

68. Glykys J, Duquette E, Rahmati N, Duquette K, Staley KJ. Mannitol decreases neocortical epileptiform activity during early brain development via cotransport of chloride and water. *Neurobiology of Disease* 2019;125:163–175.

69. Dzhala VI et al. Progressive NKCC1-dependent neuronal chloride accumulation during neonatal seizures. *J Neurosci* 2010;30(35):11745–11761.

70. Glykys J et al. Local Impermeant Anions Establish the Neuronal Chloride Concentration. *Science* 2014;343(6171):670–675.

71. Rahmati N et al. Unique Actions of GABA Arising from Cytoplasmic Chloride Microdomains. *J. Neurosci.* 2021;41(23):4957–4975.

72. Graham RT et al. Optogenetic stimulation reveals a latent tipping point in cortical networks during ictogenesis. *Brain* 2022;awac487.

73. Inoue H, Mori S-I, Morishima S, Okada Y. Volume-sensitive chloride channels in mouse cortical neurons: characterization and role in volume regulation. *Eur J Neurosci* 2005;21(6):1648–1658.

74. Lambert IH, Hoffmann EK, Pedersen SF. Cell volume regulation: physiology and pathophysiology. *Acta Physiol (Oxf)* 2008;194(4):255–282.

75. Hoffmann EK, Lambert IH, Pedersen SF. Physiology of Cell Volume Regulation in Vertebrates. *Physiological Reviews* 2009;89(1):193–277.

76. Holtmaat A et al. Long-term, high-resolution imaging in the mouse neocortex through a chronic cranial window. *Nat Protoc* 2009;4(8):1128–1144.

Figures and legends

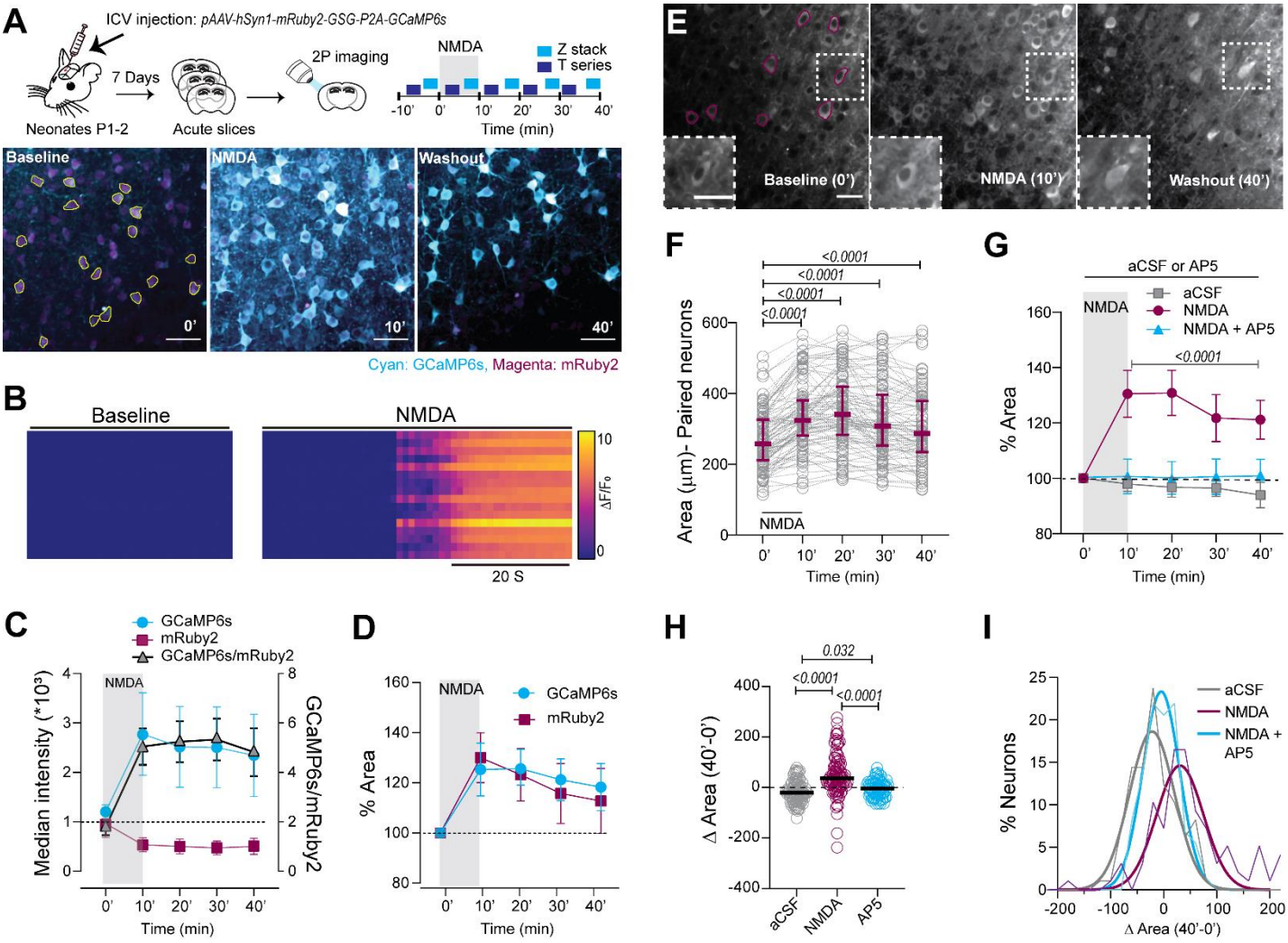

Figure 1: Brief NMDA perfusion induces long-term neuronal swelling and increases neuronal Ca^{2+} in the neonatal neocortex.

(A) *Top:* neuron-specific viral delivery of a stable fluorophore (mRuby2) and a Ca^{2+} sensor (GCaMP6s) along with the experimental design describing the acquisitions of z-stacks and single-plane t-series. *Bottom:* representative dual-color images of mRuby2 and GCaMP6s expressing cortical neurons before (0'), during (10'), and after (40') NMDA application, with ANMAF-generated ROIs overlayed on the baseline image. **(B)** Synchronized Ca^{2+} activity ($\Delta F/F_0$) heatmap of neurons during NMDA application (n=27 neurons from 1 slice, **Video 1)**. **(C)** Long-lasting increase in GCaMP6s

signals along with **(D)** persistent elevation of the neuronal area over 40' after NMDA treatment, detected using both GCaMP6s and mRuby2 (n [mice: slices: neurons] =2:3:54). **(E)** Representative images of GCaMP6s-expressing cortical neurons at different time points (0', 10', and 40') using transgenic Thy1-GCaMP6s mice. *Insets*: A single neuron at higher magnification shows persistent elevation in Ca^{2+}. **(F)** Matched comparisons of neuronal areas between multiple time points, showing persistent swelling in most neurons. Statistical analysis: one-way ANOVA with Dunnett's post-test, $F(2.8, 261) = 49.6$, $p<0.0001$. **(G)** Significant and persistent increase in the neuronal areas after NMDA application, prevented by AP5 treatment. Statistical analysis: two-way ANOVA with Tukey's post-test, $F(8, 1020) = 12.1$, $p<0.0001$; n = 5:8:97 (aCSF), n = 6:11:97 (NMDA), n = 3:5:73 (AP5). **(H)** Increase in areas of paired neurons at 40' after NMDA application (Δ Area, 40' minus 0'), rescued partially by AP5. Statistical analysis: Kruskal-Wallis test with Dunn's post-test, $p<0.0001$, 'n' same as **Figure1f**. **(I)** Distribution of total neuronal Δ Area at 40', (n: aCSF=579 neurons, NMDA=315, AP5=123). Data represented as mean ± 95% CI (parametric data) or median ± IQR (non-parametric data). Scale bar: 50 µm. See **also Supplemental Figure 1 and 2**.

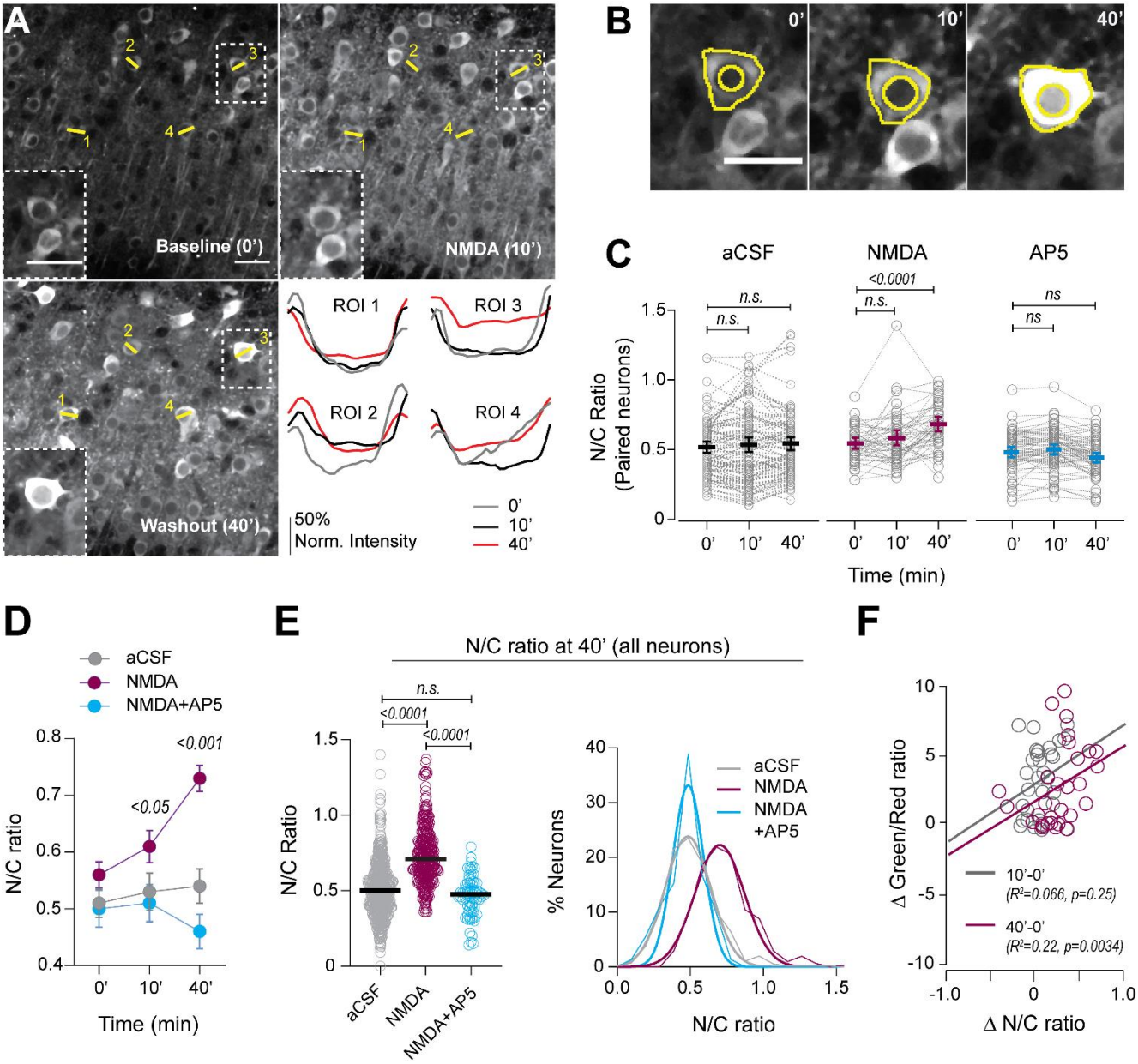

Figure 2: NMDA-mediated excitotoxic injury causes an increase in nuclear GCaMP6s fluorescence in neonatal pyramidal neurons.

(A) Neurons expressing GCaMP6s during baseline (0'), NMDA perfusion (10'), and washout (40'). *Inserts:* single magnified neuron showing long-lasting edema and increased nuclear and somatic GCaMP6s signal following NMDA application. Due to the swelling of extracellular space, one of the neurons in the box is out of the imaging plane. *Bottom right:* Representative traces showing normalized GCaMP6s intensity across linear ROIs drawn across somatic and nuclear compartments at multiple time points. **(B)** Overlays of nuclear ROIs (circular ROI at the centroid) and cytosolic ROIs (XOR:

ANMAF-generated ROI minus nuclear ROI) used to generate compartmentalized Ca^{2+} signal intensities. **(C)** Matched comparisons of nuclear to cytosolic Ca^{2+} ratios (N/C ratios) across time in multiple conditions. Statistical analysis for NMDA: RM one-way ANOVA with Dunnett's post-test, F (1.94, 93) =12.8, p<0.0001, for aCSF alone: Freidman's test with Dunn's post-test, p=0.12, for AP5: Freidman's test with Dunn's post-test, p=0.032, n same as **Figure1f**. **(D)** Comparison between groups shows an increased N/C ratio at 10' followed by a further increase at 40'. Statistical analysis: two-way ANOVA with Tukey's post-test, F (4, 1044) =12.6, p<0.0001, n as **Figure1f**. **(E)** *Left:* Changes in N/C ratios using the total number of neurons at 40' after NMDA application, rescued by AP5 application. Spearman's correlation: Kruskal Wallis test with Dunn's post-test, p<0.0001, n same as **Figure1l**. *Right:* distribution of N/C ratios at 40' (all neurons). **(F)** Significant Spearman's correlation between Δ Green/Red ratio and Δ N/C ratios at 40', but not at 10' (n=54). Data represented as mean ± 95% CI (parametric data) or median ± IQR (non-parametric data). Scale bar: 50 µm. See also **Supplemental Figure 2-5**.

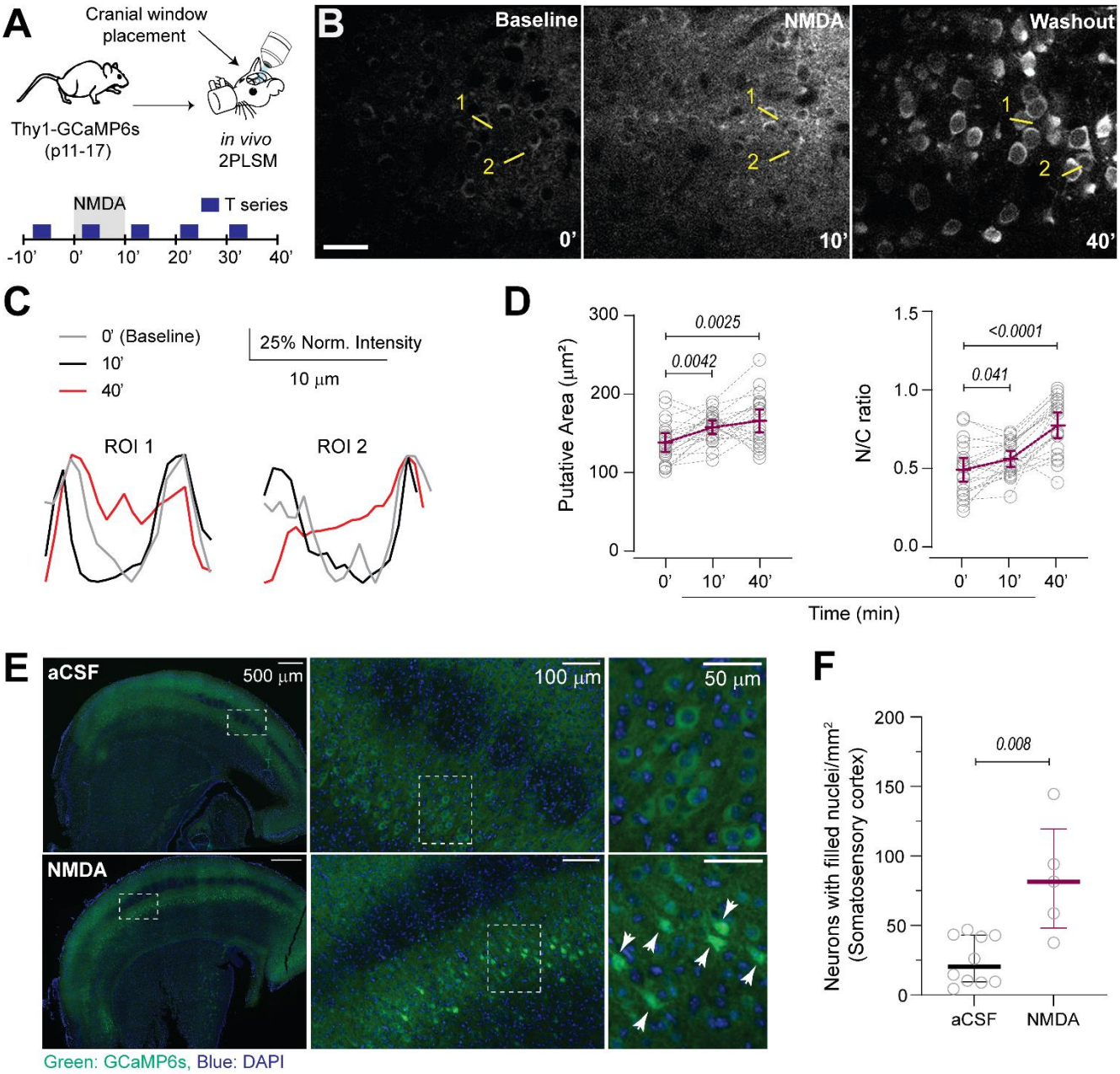

Figure 3: Excitotoxicity-induced nuclear translocation of GCaMP6s fluorescence *in vivo* and in post-fixed brain tissue.

(A) Schematic depicting cranial window placement and *in vivo* 2PLSM. **(B)** Neurons expressing GCaMP6s during baseline (0'), NMDA perfusion (10'), and washout (40') *in vivo* (**Video 2**). **(C)** Normalized GCaMP6s intensity across linear ROIs drawn across somatic and nuclear compartments at multiple time points from **3b**. **(D)** *Left*: putative areas in matched neurons enlarged at 10' and 40' after NMDA. Statistical analysis: RM one-way ANOVA with Dunnett's post-test, F (1.79, 35.8) =8.6,

p=0.0013, n (mice: matched neurons) =4:24. *Right*: The N/C ratios (matched neurons) increased at 10' and more so at 40'. Statistical analysis: RM one-way ANOVA with Dunnett's post-test, F (1.86, 37.1) =46.3, p<0.0001, n=4:24. **(E)** Post-fixed slices (4% PFA) representing aCSF control (*top*) and NMDA treatment (*bottom*) showing GCaMP6s signal in green and nuclear DAPI staining in blue. In-sets, higher magnification. Arrowheads: neurons with filled nuclei. **(F)** Increased number of neurons with filled nuclei after NMDA treatment. Statistical analysis: Mann-Whitney test, n (slices): aCSF=10, NMDA=6. Data represented as mean ± 95% CI (parametric data) or median ± IQR (non-parametric data). Scale bar: 50 µm **(B)** and 100 µm **(E and F)**.

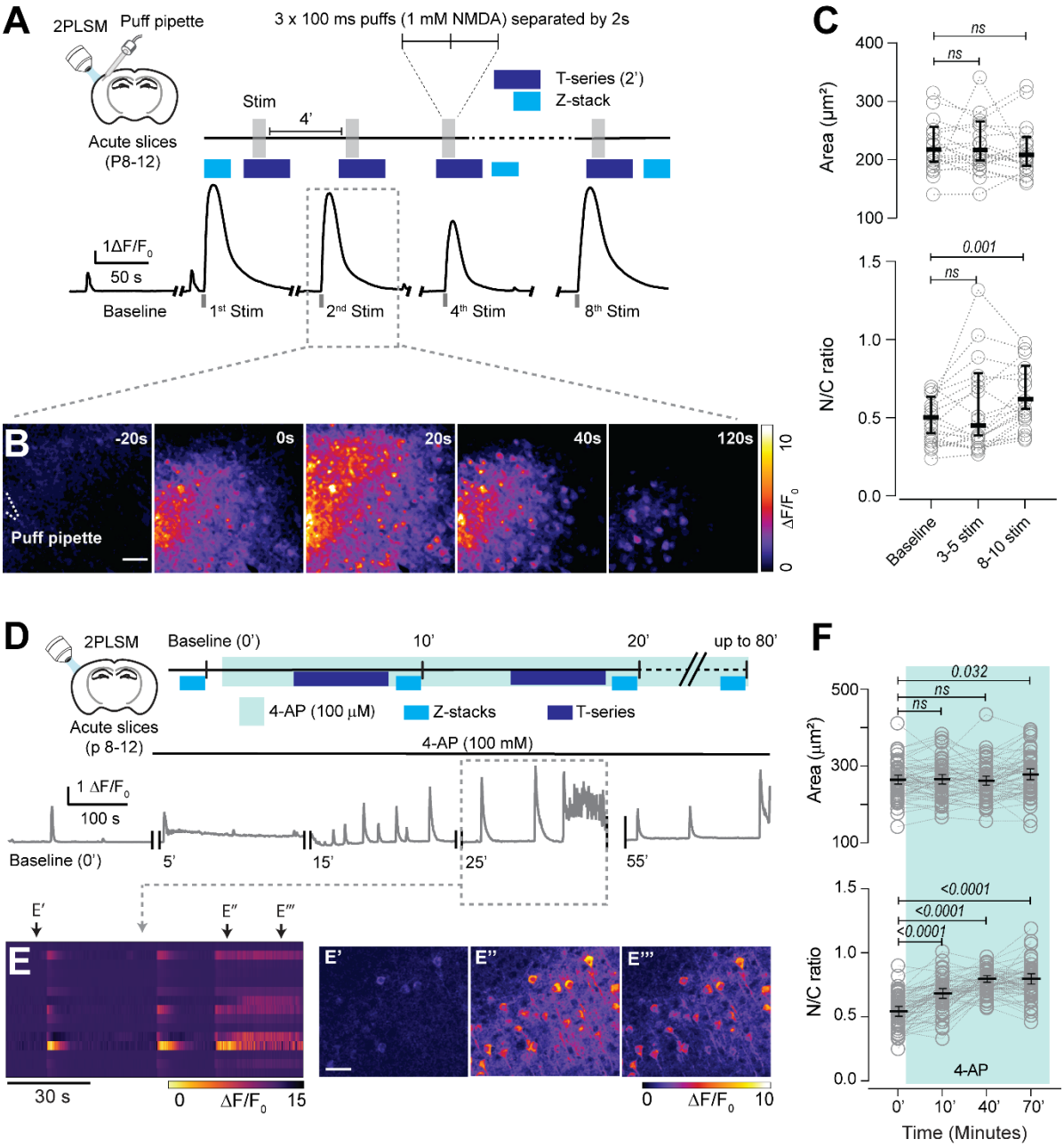

Figure 4: GCaMP6s nuclear translocation following repeated network stimulation and seizure-like events in the neonatal neocortex.

(A), *Top*: experimental design. *Bottom:* Stimulus evoked whole-field Ca^{2+} transients. **(B)** Real-time spatial propagation of a single evoked Ca^{2+} transient (**Video 4**). **(C)** *Top*: No increase in the neuronal area following multiple stimuli. Statistical analysis: Friedman's test with Dunn's post-test, P=0.7, (mice: slices: neurons) n=3:4:26. *Bottom*: N/C ratio is unchanged after 3-5 stimuli but significantly increased after 8 to 10 stimuli. Statistical analysis: Friedman test with Dunn's post-test, p=0.0013,

n=3:4:26. **(D)** *Top*: experimental design. *Bottom*: Representative whole-field trace of Ca^{2+} transients ($\Delta F/F_0$) during seizure-like activity during 4-AP perfusion (**Video 5**). **(E)** *Left*: neuronal synchronized Ca^{2+} activity heatmap ($\Delta F/F_0$) during 4-AP (2', 21 neurons). *Right:* elevation of GCaMP6s signal in neurons before and during a seizure-like event. **(F)** *Top:* neurons swell after prolonged 4-AP perfusion. Statistical analysis: RM one-way ANOVA with Dunnett's post-test, F (2.92, 175) =4.11, p=0.0081, n=3:5:64. *Bottom*: sustained increase in N/C ratio beginning 10' after 4-AP, lasting up to 70'. Statistical analysis: RM one-way ANOVA with Dunnett's post-test, F(2.83, 170)=80.5, p<0.0001, n=3:5:64. Data represented as mean ± 95% CI (parametric data) or median ± IQR (non-parametric data). Scale bar: 50 µm. See also **Supplemental Figure 6**.

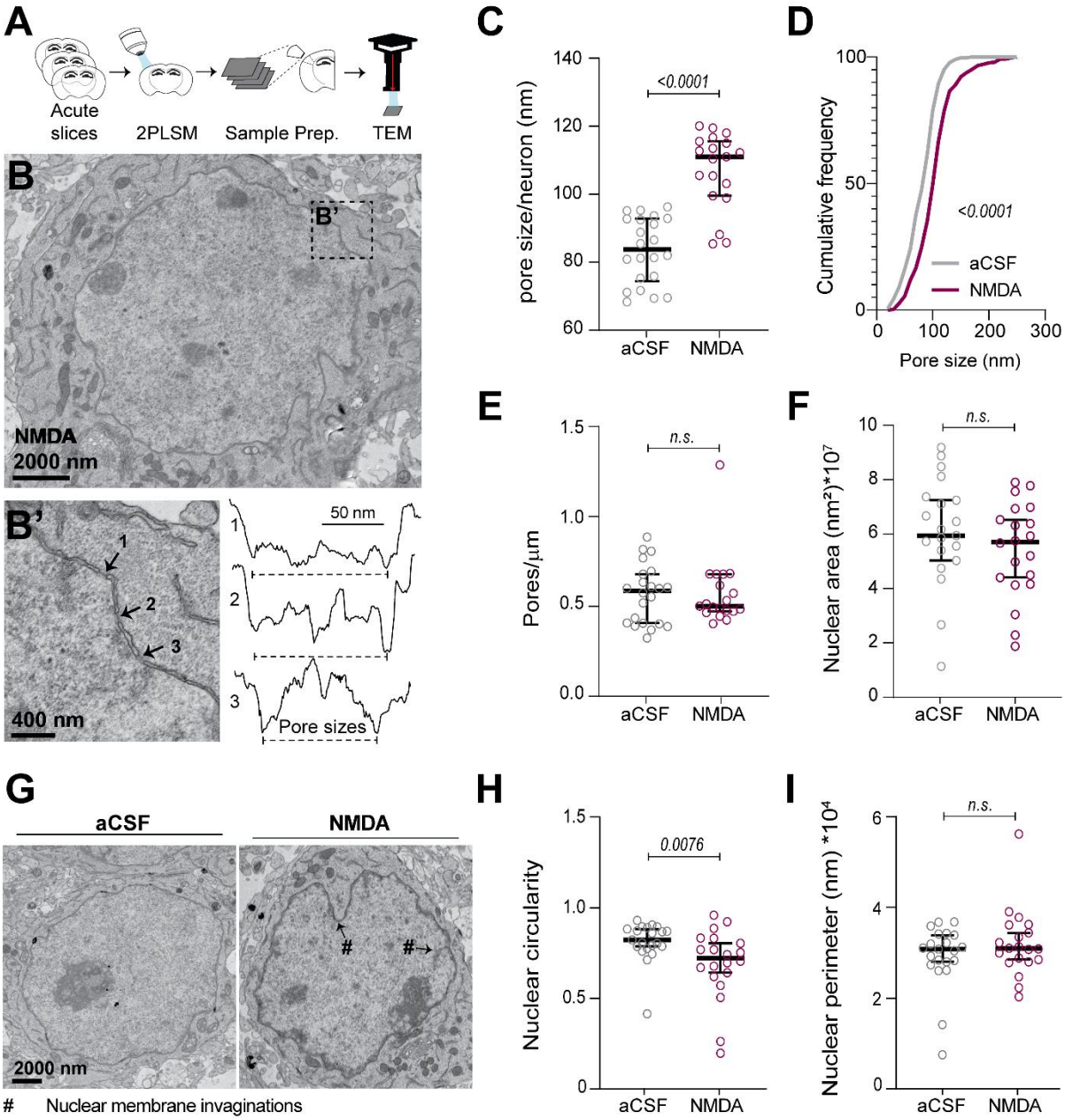

Figure 5: NMDA-excitotoxicity renders nuclear membranes more permeable by increasing nuclear pore size.

(A) Experimental design. **(B)** Transmitted electron microscopy (TEM) image of an entire neuronal nucleus (left) along with a magnification showing multiple nuclear pores (**b'**, 25,000x, arrowheads) along with normalized electron density across linear ROIs (**B'**) drawn over the nuclear pores and adjacent membrane. Pore size was calculated as the distance between the first and last peaks. **(C)** NMDA increased the average neuronal nuclear pore size. Statistical analysis: Mann-Whitney test, n (slices:

tissue samples: nuclei): aCSF=2:4:22, NMDA=2:3:19. **(D)** NMDA shifted the pore size distribution with no change in **(E)** pore density or **(F)** nuclear area. Statistical analysis: 2-sample KS test, n (total pores): aCSF=343, NMDA=406. **(G)** TEM images showing nuclear invaginations (marked as #) following aCSF alone and NMDA treatments. **(H)** Nuclear circularity decreased with NMDA due to increased nuclear membrane invaginations (Unpaired t-test) with no significant change in **(I)** nuclear perimeter (Mann-Whitney test). Data represented as mean ± 95% CI (parametric data) or median ± IQR (non-parametric data).

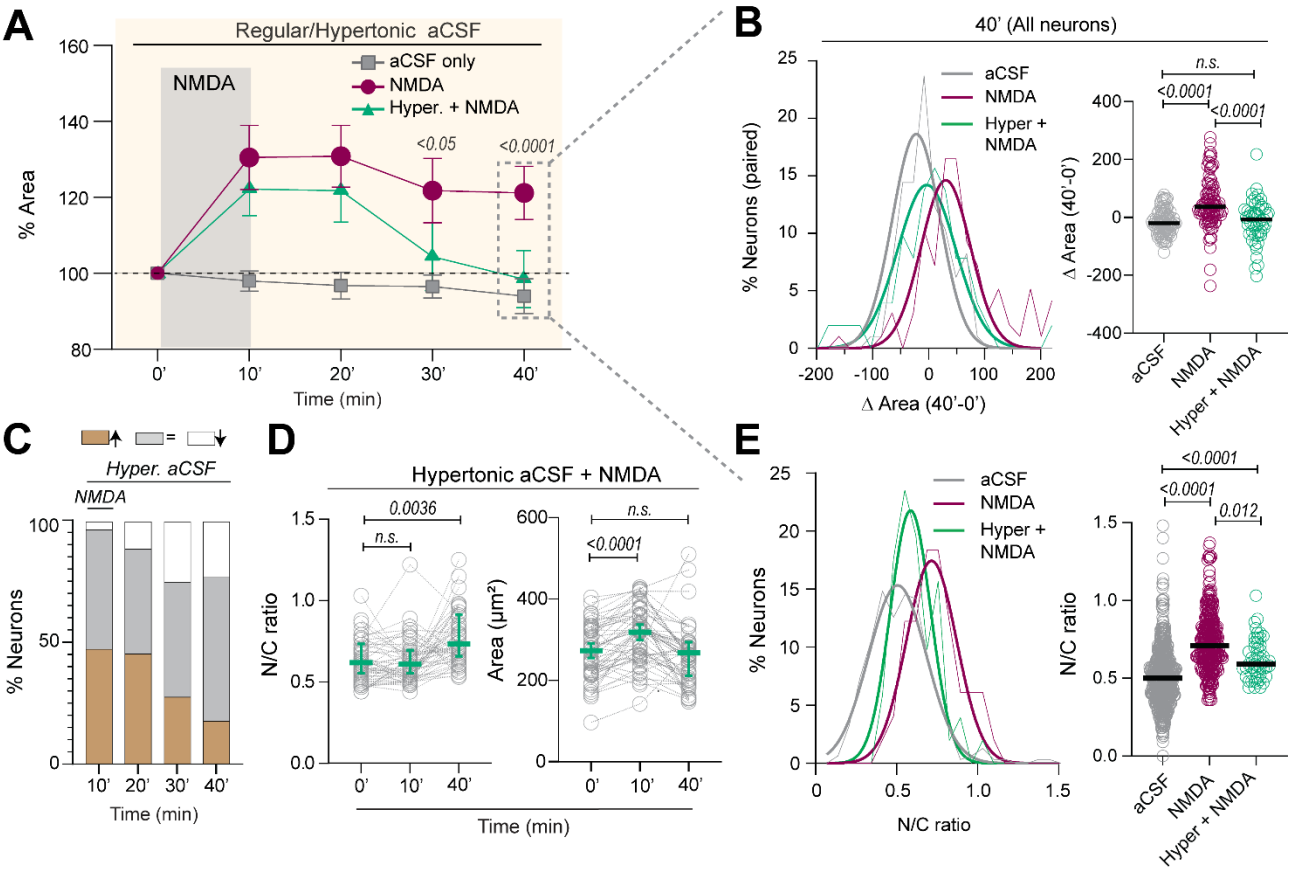

Figure 6: Mitigating long-term neuronal excitotoxic edema does not prevent the persistent increase in the N/C ratio.

(A) NMDA-induced long-term swelling is rescued with hypertonic aCSF (+40 mOsm, green) at 30' and 40'. Statistical analysis: two-way ANOVA with Tukey's post-test, F (8, 915) =8.78, p<0.0001, n(mice: slices: neurons) for aCSF = 4:6:75, for NMDA = 5:8:60, for hypertonic aCSF + NMDA = 3:5:54. **(B)** *Left*: difference in areas distribution at 40' (40' minus 0') in aCSF, after 10' NMDA, and with hypertonic aCSF. *Right*: Hypertonic aCSF Δ Areas at 40' (40'-0'). Statistical analysis: Kruskal-Wallis test with Dunn's post-test, P<0.0001, aCSF = 312, NMDA = 234, Hypertonic aCSF. + NMDA = 109. **(C)** Proportions (%) of neurons with a change in their areas (1*SD difference to baseline) at different time points with NMDA + hypertonic aCSF treatment. The percentage of swollen neurons was reduced with NMDA + hypertonic aCSF treatment (30.3±38.8) compared to NMDA alone (15.4±26.1; **Supplemental Figure 7C**). (**D)** Neuronal areas and N/C ratios measured from matched neurons

across time. Hypertonic conditions prevented NMDA-induced neuronal swelling at 40' but failed to prevent an increase in the N/C ratio. Statistical analysis: *left,* RM one-way ANOVA with Dunnett's post-test, $F(1.62, 81) = 18.6$, $p<0.001$, n=3:5:54, *right*, Friedman's test with Dunn's test, $p=0.0002$. **(E)** N/C ratio distributions from all neurons at 40'. Statistical analysis: Kruskal-Wallis test with Dunn's post-test, $p<0.0001$. Data represented as mean ± 95% CI (parametric data) or median ± IQR (non-parametric data). See also **Supplemental Figure 7 and 8**.

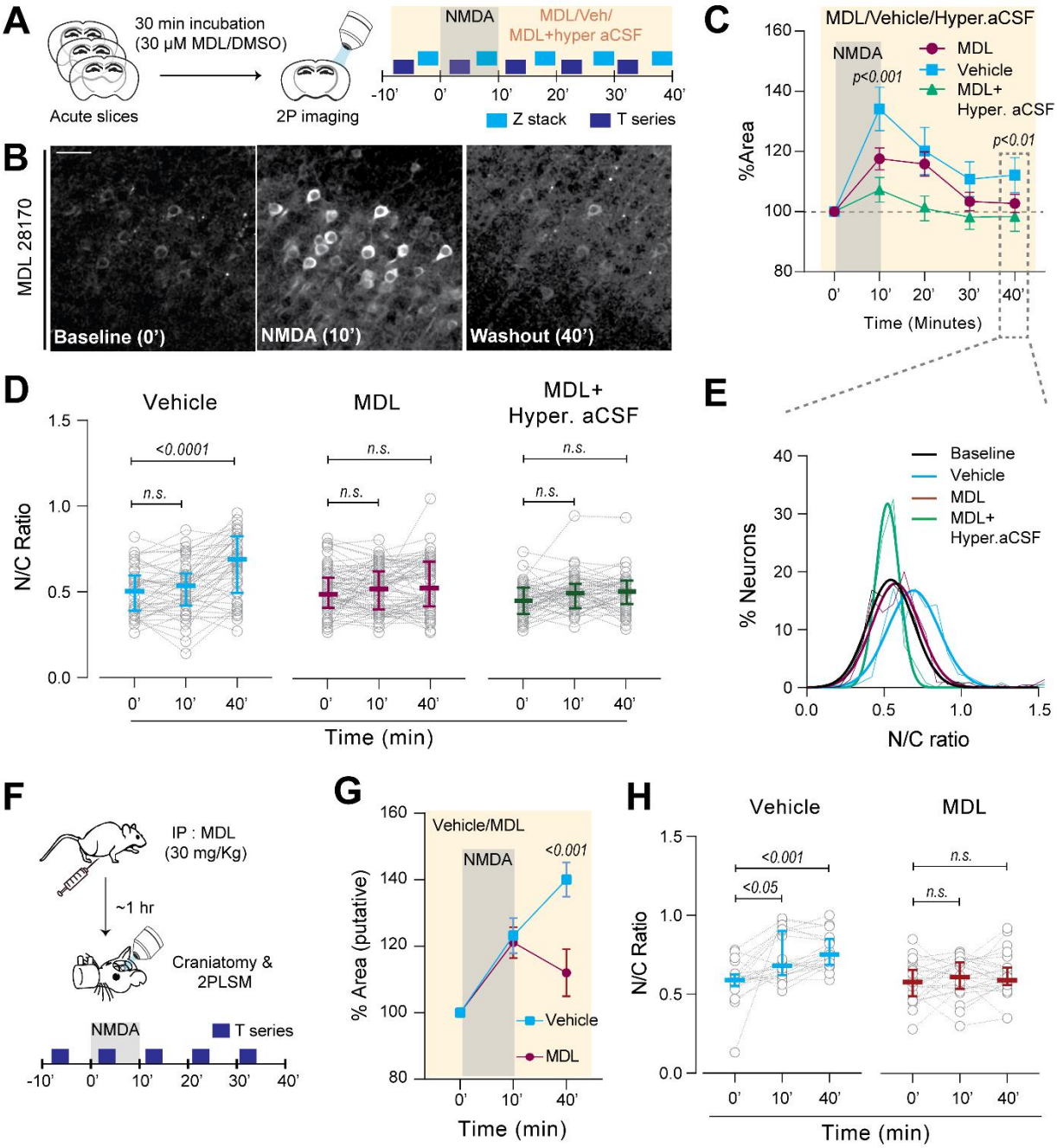

Figure 7: Calpain inhibition prevents nuclear translocation of GCaMP6s after NMDA-induced excitotoxic injury.

(A) Experimental design. (**B)** Neurons expressing GCaMP6s during baseline (0'), NMDA perfusion (10'), and washout (40') after calpain inhibition. (**C)** NMDA-induced neuronal swelling decreased with a calpain inhibitor (MDL 28170) compared to vehicle. Statistical analysis: Two-way ANOVA, F (8, 825) =5.58, p<0.0001, Tukey's post-test at 40' p<0.01, n(mice: slices: neurons), vehicle = 3:4:49, MDL =4:7:72. MDL + hypertonic aCSF treatment further reduced NMDA-induced swelling at 40'

($p<0.0001$; n=3:4:47). (**D)** N/C ratios from matched neurons across time. Calpain inhibition prevented the increase in the N/C ratio. Statistical analysis: Friedman's test with Dunn's post-test, Vehicle: $p<0.0001$; MDL: $p=0.06$; MDL + Hypertonic aCSF: $p=0.11$. **(E)** Frequency distribution of N/C ratios from all neurons shows an increase in the vehicle compared to baseline but not in MDL and MDL + hypertonic aCSF groups. **(F)** Schematic showing MDL pretreatment (IP: 30mg/Kg) followed by 2P imaging *in vivo*. **(G)** NMDA-induced neuronal swelling was reduced by a single MDL dose at 40'. Statistical analysis: Two-way ANOVA with Tukey's post-test, $F (2, 132) =5.6$, $p=0.0046$), n (mice: slices: neurons), vehicle = 2:14, MDL =4:18. **(H)** *In vivo* N/C ratios from matched neurons across time. MDL prevented N/C ratio increase. Statistical analysis: RM one-way ANOVAs with Dunnett's post-test, vehicle: $F (1.21, 24.2) =14.0$, $p=0.0005$; MDL: $F (1.7, 40.7) =0.72$, $p=0.47$. Data represented as mean ± 95% CI (parametric data) or median ± IQR (non-parametric data). Scale bar: 50 µm.